SMOS Level-2 Soil Moisture Product Evaluation in Rain-Fed Croplands of the Pampean Region of Argentina

Raquel Niclòs, Raúl Rivas, Vicente García-Santos, Carolina Doña, Enric Valor, Mauro Holzman, Martín Bayala, Facundo Carmona, Dora Ocampo, Álvaro Soldano, Marc Thibeault, Vicente Caselles, and Juan M. Sánchez

***Abstract*—A field campaign was carried out to evaluate the Soil Moisture (SM) MIR_SMUDP2 product (v5.51) generated from the data of the Microwave Imaging Radiometer using Aperture Synthesis (MIRAS) aboard the Soil Moisture and Ocean Salinity (SMOS) mission. The study area was the Pampean Region of Argentina, which was selected because it is a vast area of flatlands containing quite homogeneous rain-fed croplands, which are considered SMOS nominal land uses and hardly affected by radio-frequency interference contamination. Transects of ground handheld SM measurements were performed using ThetaProbe ML2x probes within four Icosahedral Snyder Equal Area Earth (ISEA) grid nodes, where permanent SM stations are located. The campaign results showed a negative bias of -0.02 $\mathbf{m^3m^{-3}}$ between concurrent SMOS data and ground SM measurements, which means a slight SMOS underestimation, and a standard deviation of ± 0.06 $\mathbf{m^3m^{-3}}$. Additionally, a good correlation was obtained between the handheld SM measurements taken during the campaign and the permanent SM station data within a node, which pointed out that the station data could be used as reference data to evaluate the SMOS product over a longer temporal period. SMOS-retrieved data were also compared with station mean SM values from 2012 to 2014. A general SMOS underestimation of -0.05 $\mathbf{m^3m^{-3}}$ was observed, with a standard deviation of ± 0.04 $\mathbf{m^3m^{-3}}$, which yields an uncertainty of ± 0.07 $\mathbf{m^3m^{-3}}$ for the SMOS product. Although the random error meets the SMOS mission's goal of ± 0.04 $\mathbf{m^3m^{-3}}$, the product overall uncertainty is higher than that due to the significant dry bias, which is also found in other regions of the world.**

***Index Terms*—Ground measurements, product evaluation, Soil Moisture and Ocean Salinity (SMOS), soil moisture (SM).**

I. Introduction

THE European Space Agency's (ESA) Soil Moisture and Ocean Salinity (SMOS) mission was launched in November 2009 as part of the ESA's Living Planet Programme [1], [2]. Developed to further understand the Earth's water cycle, the second Earth Explorer Opportunity mission aims to contribute to weather and extreme event forecasting by providing global soil moisture (SM) data over land and salinity over oceans [1], [2]. The Microwave Imaging Radiometer with Aperture Synthesis (MIRAS) instrument aboard the SMOS mission is a passive radiometer that detects microwave radiation emitted from the Earth's surface with a frequency of 1.41 GHz (wavelength of 21.2 cm; L-band). SMOS has a sun-synchronous quasi-circular orbit, with a 23-day repeat cycle, although a complete set of global measurements corresponds to an approximate three-day temporal resolution using both ascending and descending passes [1]. The average spatial resolution for SMOS-MIRAS (3-dB half-power beamwidth) is approximately 40 km. However, ground instantaneous field of views (GIFOVs) varies between roughly 27 km at nadir and 55 km at the edges of the observation swath [3].

The principle of the SMOS Level-2 (L2) retrieval algorithm over land is to exploit multiangular and bipolarization data in order to simultaneously retrieve two main surface parameters: the SM and the vegetation optical depth, which is related to the vegetation biomass [4]. Since multiangular data (i.e., with different GIFOVs) are used in the retrieval algorithm, SMOS L2 data are represented over the fixed ISEA-4H9 grid, with equally spaced nodes at 14.989 km, which are usually referred to as discrete global grid (DGG) nodes [3], [4]. SMOS SM is provided as an SM L2 User Data Product (MIR_SMUDP2) [3], [5]. The SMOS L-band has a typical contributing depth of 2–5 cm [1], [6], [7], which results in a more stable SM value over the diurnal cycle than SM from other sensors with shorter wavelengths (e.g., AMSR-E X-band channel, with a frequency

Manuscript received August 1, 2014; revised February 27, 2015 and May 29, 2015; accepted July 11, 2015. This work was supported in part by the Spanish Ministerio de Ciencia e Innovación y Ministerio de Economía y Competitividad under Project CIUCISMOS CGL2011-13579-E, Project CGL2011-30433-C02-02, and Project CGL2013-46862-C2-1/2-P, by Argentinean Comisión Nacional de Actividades Espaciales under the CONAE No107/09 Project, and by the Comisión de Investigaciones Científicas de la provincia de Buenos Aires (CIC). The work of R. Niclòs was supported by the Spanish Ministerio de Ciencia e Innovación y Ministerio de Economía y Competitividad under the "Ramón y Cajal" RYC-2010-06213 Research Contract. The work of V. García-Santos was supported by the Generalitat Valenciana under the "Vali+D" APOSTD/2015/033 postdoctoral contract.

R. Niclòs, V. García-Santos, C. Doña, E. Valor, and V. Caselles are with Department of Earth Physics and Thermodynamics, University of Valencia, 46100 Burjassot, Spain (e-mail: raquel.niclos@uv.es; vicente.garcia-santos@uv.es; carolina.dona@uv.es; enric.valor@uv.es; vicente.caselles@uv.es).

R. Rivas, M. Holzman, M. Bayala, F. Carmona, and D. Ocampo are with the Instituto de Hidrología de Llanuras, B7300 Buenos Aires, Argentina (e-mail: rrivas@rec.unicen.edu.ar; mauroh@faa.unicen.edu.ar; martin.bayala@rec.unicen.edu.ar; facundo.carmona@rec.unicen.edu.ar; dora.ocampo@rec.unicen.edu.ar).

A. Soldano and M. Thibeault are with the Comisión Nacional de Actividades Espaciales, 1063 Buenos Aires, Argentina (e-mail: asoldano@conae.gov.ar; mthibeault@conae.gov.ar).

J. M. Sánchez is with the Applied Physics Department, School of Mining and Industrial Engineering, University of Castilla-La Mancha, 13400 Almadén, Spain (e-mail: JuanManuel.Sanchez@uclm.es).

Color versions of one or more of the figures in this paper are available online at http://ieeexplore.ieee.org.

Digital Object Identifier 10.1109/TGRS.2015.2460332

of 10.65 GHz and a wavelength of 2.8 cm, used in most AMSR-E SM algorithms) [8]. In addition, the effects of vegetation (in particular attenuation), as well as surface roughness and atmosphere, are less significant at longer wavelengths [8]. A detailed description of the MIR_SMUDP2 algorithm used to retrieve SM from the SMOS data is provided in [1], [3], and [5]. Using an initial SM guess and auxiliary data, brightness temperatures are modeled by means of the L-band Microwave Emission of the Biosphere (L-MEB) model [9]. SM is then retrieved by minimizing a cost function between modeled and SMOS measured multiangular brightness temperatures [3], [4].

Although the aim of the SMOS mission is to provide volumetric SM values within ± 0.04 m^3m^{-3} [4], some previous papers have shown substantially higher uncertainties. Dall'Amico *et al.* [10] found a SMOS data dry bias between 0.11 and 0.3 m^3m^{-3} in the upper Danube catchment in South Germany, and Gherboudj *et al.* [11] observed a SMOS SM underestimation with an RMSE varying from 0.15 to 0.18 m^3m^{-3} for agricultural and boreal forest sites in Canada. However, other papers pointed out that SMOS SM estimates are approaching the level of performance anticipated [8], [12]–[14], mainly for nominal land covers, i.e., bare soils or low vegetation (grass and crops with vegetation heights not exceeding 1 to 2 m, by opposition to trees) [3], [11].

In this paper, a specifically designed field campaign was carried out to test the SMOS MIR_SMUDP2 product in extensive rain-fed croplands in the Pampean Region of Argentina (PRA). In such rain-fed croplands, where most of world food grain production is obtained (with a world harvested extension of 516 million ha among wheat, maize, and soybean crops in 2013 according to FAO; http://faostat3.fao.org/), an accurate monitoring of SM spatial and temporal variability is essential to estimate crop yield (since the main cause of crop yield instability is the dependence on SM variability), plan the planting, and evaluate the regional water and energy balances [15], with SM being a key input variable in water balance models. Since these crops play a considerable role in global food security, their preharvest yield prediction is fundamental for supporting export–import policies. In addition, no evaluation of the SMOS SM product were carried out before in South America [14], where the radio-frequency interference (RFI) contamination is rather weak (both for ascending and descending overpasses), as can be observed in http://www.cesbio.ups-tlse.fr/SMOS_blog/smos_rfi. RFI deteriorates the SMOS data quality with a significant impact in some regions of the world, e.g., in Europe [11], [12].

We evaluated the version 5.51 of the SMOS MIR_SMUDP2 product. Most of the aforementioned references used product versions previous to the v5.51, and the aim of this paper is to estimate the soundness of this operational version to monitor the SM variability in rain-fed croplands. The main difference between version 5 and the previous version 4 is an improvement of the RFI detection algorithm, which uses a temperature threshold linked to the surface expected emissivity rather than a fixed threshold [5]. The main difference between v5.51 (v5.50) and v5.01 (v5.00) is the change of the dielectric constant model, from the Dobson Model with Peplinski's modification to the Mironov formulation [5], [16], with the aim of improving SM estimates, with better and more successful retrievals over dry warm surfaces, and reducing extreme values of SM.

TABLE I
EXPERIMENTAL SITES CORRESPONDING TO FOUR SMOS DGG NODES. SAMPLING DAYS CONCURRENT WITH SMOS OVERPASSES, BOTH ASCENDING (10:30–11:00 UTC; 7:30–8:00 LOCAL TIME) AND DESCENDING (21:30–22:00 UTC; 18:30–19:00 LOCAL TIME), DURING THE FIELD CAMPAIGN IN FEBRUARY 2013

Site name	SMOS DGG ID	Geographic latitude	Geographic longitude	Sampling days (February, 2013)
SN	6025215	32° 58' 15.6"S	62° 31' 04.8"W	5, 7, 15
BE	6023165	32° 30' 00.0"S	62° 47' 31.2"W	10, 17, 18
MA	6020086	32° 00' 50.4"S	63° 42' 18.0"W	12
TA	6047263	37° 17' 52.8"S	58° 52' 51.6"W	20

The experimental campaign was performed in Summer 2013, i.e., with quite dry and warm surfaces in the study region. During the campaign, handheld SM measurements were carried out along transects, which were first used to test the MIR_SMUDP2 product. Then, continuous SM data logged by stations permanently installed in the study region were additionally used to extend the evaluation period to two and a half years (2012–2014). Since the difference between SMOS ascending and descending retrievals remains unclear [8], [13], and [17], evaluation results of both ascending and descending overpass data were assessed separately to investigate possible differences on the SM product accuracy depending on acquisition time.

This paper is organized as follows. Section II describes the experimental sites, the measurement strategy, the instrumentation, and the SMOS and ground data comparison methodology. Section III shows results and discussion of the product evaluation when using handheld SM measurements acquired during the campaign and the SM time series collected by the stations as reference data. Finally, Section IV summarizes the main conclusions drawn from this paper.

II. EXPERIMENTAL SITES, METHODOLOGY, AND INSTRUMENTATION

Experimental sites were located in the Córdoba and Buenos Aires provinces. Geographically, the PRA spans a vast area of flatlands (with slopes lower than 1%), avoiding strong topography effects [18], containing mainly homogeneous soybean cultivations, with scattered maize crops. The land cover of this area corresponds mainly to rain-fed croplands, as observed from the ESA's GlobCover land cover map [19]. The height of vegetation varies from 1 to 2 m; thus, land cover can be considered nominal land cover (low vegetation), for which SMOS L2 products provide reliable data for a nominal retrieval configuration. Handheld SM measurements were carried out within the areas covered by four specific ISEA-4H9 DGG nodes in the described area during the campaign. Table I shows the assigned names to the SMOS nodes, their DGG IDs, and their central geographical coordinates. The four nodes cover extensive agricultural areas with prevalence of soybean cultivations. The test sites were selected by taking as reference the locations of stations permanently installed for the continuous acquisition of SM data. Fig. 1 shows the locations of the selected

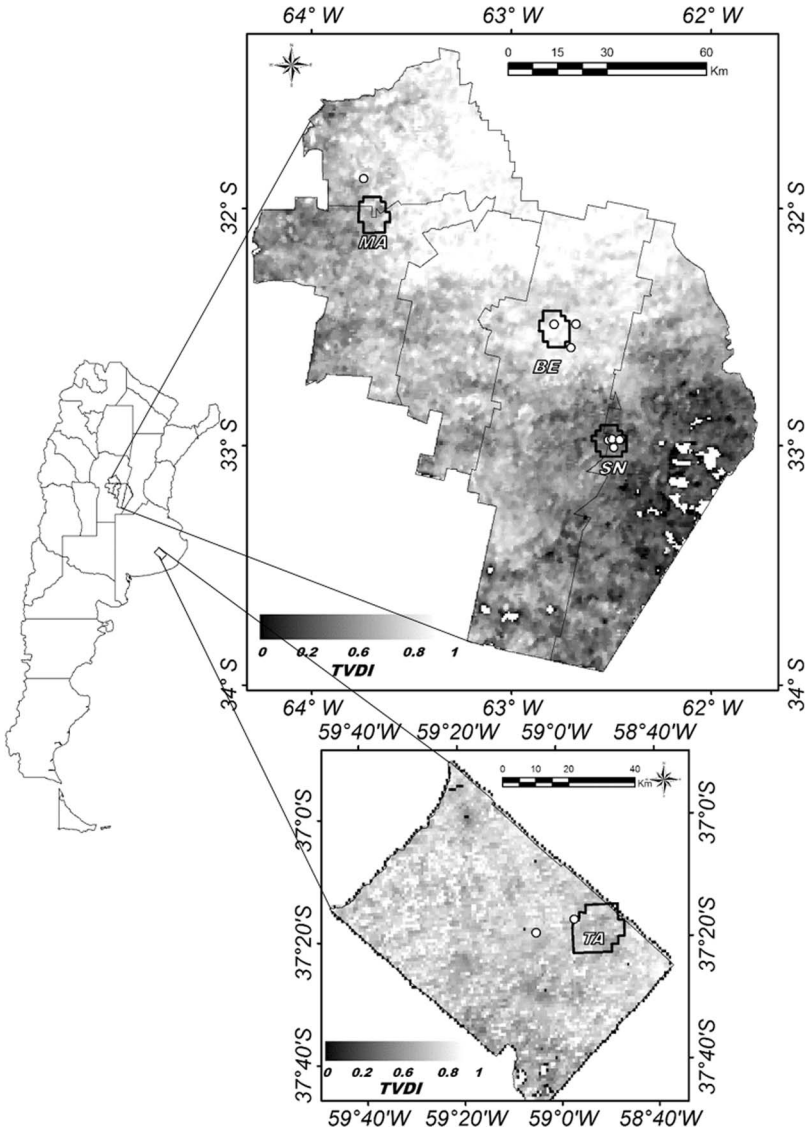

Fig. 1. Locations of the selected DGG nodes (black polygons) and the permanent stations near or inside them (white circles) in the PRA, shown over a TVDI map generated from MODIS products (10–25 February 2012).

DGG nodes and the permanent stations near or inside them. They have been shown over a map of temperature vegetation dryness index (TVDI) [15], which is strongly correlated with subsurface SM, generated from EOS-MODIS data. The stations are property of the Argentinean CONAE, Instituto Nacional de Tecnología Agropecuaria (INTA, National Institute of Farming Technology), and Instituto de Hidrología de Llanuras (IHLLA, Plain Hydrology Institute). There are five stations within the SN node, with SN being the selected node with the highest number of stations inside.

A. Field Campaign

The duration of the field campaign was one month (February 2013). Table I includes the days when handheld SM measurements were taken concurrently with SMOS overpasses in the different selected nodes. Additionally, SM measurements were carried out at the nodes even when no SMOS overpasses were scheduled for the experimental sites with the aim of monitoring the SM temporal evolution.

Handheld measurements were taken along transects at the SMOS overpass times for each specific node, for both ascending (10:30–11:00 UTC; 7:30–8:00 local time) and descending overpasses (21:30–22:00 UTC; 18:30–19:00 local time). We selected six parcels (with a minimum size of 0.5×0.5 km^2) spatially distributed within each node. Although the campaign was performed in extensive flat and homogeneous rain-fed agricultural areas, the parcels were specifically selected to give representative measurements of the whole nodes by taking into account land cover, soil type, and crop fractions within each node. Soil type was analyzed using soil order and texture maps provided by INTA (http://geointa.inta.gov.ar/visor). The main textural classes (following the U.S. Department of Agriculture (USDA) Seventh Approximation Soil Classification System) in the region were loam, clay loam, and silt loam samples, and the main soil order was mollisol. Table II shows the fractions of the

TABLE II
CROP COVERS AND SOIL TEXTURAL CLASSES PER NODE AND FOR EACH EXPERIMENTAL PARCEL

Node name	Node crop cover fractions	Node soil textural class fractions	Parcel name	Parcel crop type	Parcel soil textural class	(Clay,Silt, Sand) (%)
SN	74 % soybean 26 % maize	90% loam 10% sandy loam	E	Soybean	Clay loam	(29,45,26)
			F	Maize	Loam	(25,49,26)
			G	Soybean	Loam	(21,47,32)
			H	Maize	Sandy loam	(4,50,46)
			I	Soybean	Loam	(26,45,29)
			J	Soybean	Loam	(25,46,29)
BE	79 % soybean 21 % maize	85% loam 15% silt loam	N	Soybean	Loam	(22,46,32)
			P	Maize	Loam	(17,47,36)
			T	Soybean	Loam	(11,40,49)
			Q	Soybean	Loam	(19,46,35)
			R	Soybean	Loam	(23,42,35)
			S	Soybean	Silt loam	(11,63,26)
MA	82 % soybean 18 % maize	90% loam 10% silt loam	U	Soybean	Loam	(24,39,37)
			V	Soybean	Loam	(26,39,35)
			W	Soybean	Clay loam	(28,38,34)
			X	Soybean	Silt loam	(9,59,32)
			Y	Soybean	Loam	(23,43,34)
			Z	Maize	Loam	(18,43,39)
TA	78 % soybean 22 % maize	80% loam 20% silt loam	V64	Soybean	Clay loam	(34,28,38)
			V65	Soybean	Silt loam	(13,52,35)
			V66	Soybean	Loam	(24,39,37)
			V67	Maize	Loam	(26,38,36)
			V68	Soybean	Loam	(26,36,38)
			V69	Soybean	Loam	(25,41,34)

main textural classes in each selected DGG node. Additionally, textural classes and clay, silt, and sand percentages measured in laboratory for soil samples collected in the different experimental parcels during the campaign are shown in Table II.

Soybean and maize parcels have different spectral signatures, as obtained from the reflective bands 1–5 and 7, i.e., visible and near-infrared bands (from 0.45 to 2.35 μm), of the Landsat-7 Enhanced Thematic Mapper Plus instrument (ETM+). Therefore, Landsat-7 ETM+ images of January–February 2013 were used to classify land covers and estimate node crop covers ($> 90\%$) and fractions of different crop types (mainly soybean cultivations). Crop cover fractions were checked by using official statistical data of the Ministry of Agriculture, Livestock and Fisheries (Argentina) (http://www.siia.gov.ar/) and by prior field inspections. Table II shows crop fractions estimated per node and the crop type for each experimental parcel. Additionally, as SMOS brightness temperature varies with land surface temperature (LST), EOS/Terra-MODIS MOD11_L2 LST products [20] (13:30–14:30 UTC; time of maximum LST variability) were used to test the homogeneity of the selected DGG nodes and LST standard deviations lower than 1–1.5 K were obtained for them.

Two research teams conducted measurements at the same time over one of the selected DGG nodes to constrict the measurement time to a 1-h period centered at each SMOS overpass time. Each team followed a route within the node and measured in three of the six parcels selected in the node for a period of around 15 min each one. As an example, Fig. 2 shows the SN node, outlined in white, together with the six selected parcels where measurements were done outlined in yellow and the routes followed by the two teams in blue. One team measured in parcels E, F, and G and the other measured in parcels H, I, and J. SM measurements were recorded every 10 m along three transects within each individual parcel at the same time, first moving towards the center of the parcel in parallel tracks; thereafter, one would continue straight ahead, and two of them would branch out at 90° continuing in opposite directions until the parcel borders. Measurements on crop rows and between them were collected to take into account the row crop SM variability, mainly in maize parcels. Around 30 measurements were accumulated in each transect, i.e., 90 measurements per parcel. Finally, more than 500 SM measurements were acquired per node per SMOS overpass.

Ground SM measurements were collected using Delta-T ThetaProbe ML2x SM probes [21]. The ML2x SM probe has four 60-mm-long sharpened stainless-steel rods that are inserted into the soil, providing a SM measurement within seconds. Because the dielectric constant of water ($\sim$81) is very much higher than that of soil (typically 3 to 5) and air (1) for low frequencies (i.e., up to around 2–3 GHz), the dielectric constant of a soil sample is determined primarily by its water content, which is also the basis for the SMOS SM retrieval technique. The correlation between the square root of the real part of the dielectric constant and volumetric SM content (θ_v) has been shown to be linear for many soil types and over what can be considered a practical range of water content [22]–[24]. θ_v is derived with the ML2x SM probe by responding to changes in the apparent dielectric constant, which comprises almost exclusively the dielectric constant's real part. The ML2x SM probes have been widely used for research purposes, e.g., by the International SM Network (http://ismn.geo.tuwien.ac.at/). The ML2x probe has a θ_v uncertainty of ± 0.01 $\mathrm{m^3 m^{-3}}$ after calibration to a specific soil type, and of ± 0.05 $\mathrm{m^3 m^{-3}}$ when using a generalized calibration according to the manufacturer [21].

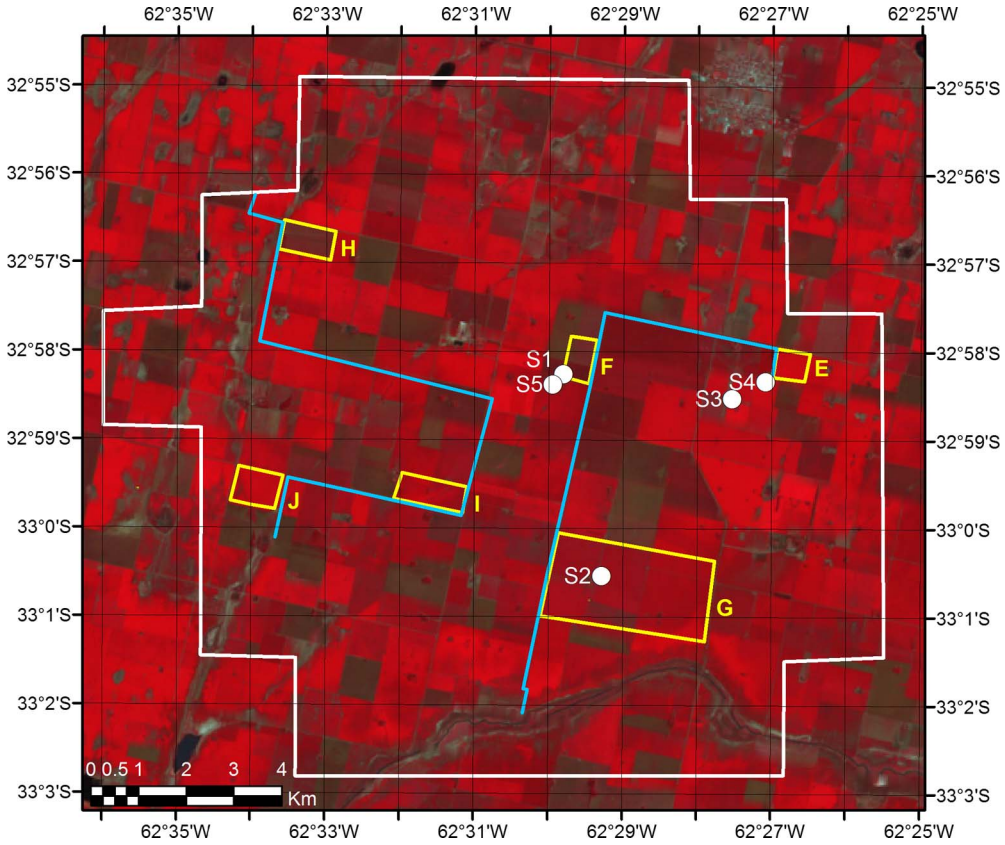

Fig. 2. SN node outlined in white, together with parcels where SM measurements were carried out along transects outlined in yellow and the two team routes in blue. White circles show the permanent station locations inside the node (S1–S5). The background image is a color composition of Landsat-7 ETM+ reflectance in band 432 on February 12, 2013. This color composition shows soybean crops in light red and maize crops in darker red.

We tested the calibration of the ML2x probes used during the campaign in the laboratory by using the gravimetric method [25], [26] and a representative variety of soil samples collected from the experimental parcels (loam, clay loam, and silt loam samples) (see Table II). The method involves measuring the mass of water present in a soil sample as a ratio of the mass of dry soil in it, and provides a result in terms of gravimetric SM content that can be converted to θ_v by considering the bulk density of the sample. The soil samples were saturated, and since that moment, they were freely dried at laboratory temperature ($\sim$20 °C). The θ_v was measured several times for each soil sample during the drying process using a ML2x probe and by measuring masses up to the lowest sample weight (constant during three days); then, the sample was artificially dried. The bulk density was measured for each sample as the ratio between dry mass, which was obtained after drying the sample in an oven at 105 °C for 48 h, and volume. Fig. 3 shows examples of the calibration results for three different samples and probes. Sample 1, which was collected in the node BE (parcel N), corresponds to a loam soil with a bulk density of 1.26 g $\cdot$ cm^{-3}; sample 2, which was collected in the node SN (parcel E), was a clay loam sample with a bulk density of 1.22 g $\cdot$ cm^{-3}; and sample 3, which was collected in the TA node (parcel V65), was a silt loam sample with a bulk density of 1.29 g $\cdot$ cm^{-3}. Similar results were obtained for the other samples and probes. Linear regression equations with the corresponding fitting errors (i.e., the standard error for the dependent variable estimate), biases between reference and ML2x probe θ_v data (i.e., the average of the differences), and RMS difference (RMSD, i.e., $(\text{bias}^2 + \text{SD}^2)^{1/2}$, with SD being the standard deviation of the differences) are included in Fig. 3. The calibration results showed accurate operations for the ML2x probes, which attain uncertainties lower than ± 0.017 m^{3}m^{-3}, in agreement with the manufacturer [21].

Additionally, the θ_v data obtained by each probe that transects in each parcel were checked by collecting soil samples in the parcels at the same time and by using the gravimetric method to obtain reference values. The main textural class of the collected soil samples in the experimental sites was loam, with some clay loam and silt loam samples (see Table II). Fig. 4 shows the θ_v reference values obtained for the different experimental parcels where samples were collected against the average values of transects measured in the parcels by three different ML2x probes (called A, B, and C) as an example. The θ_v reference values are averages for five soil samples collected in each parcel. Standard deviations for each probe transect and for the five soil samples collected per parcel were also assessed, with mean values of ± 0.02 m^{3}m^{-3} in both cases. The error bars included in Fig. 4 show those standard deviations. Fig. 4 shows that all the probe measurements follow the line 1:1 (with a linear regression coefficient of determination, r^2, of 0.89), with residuals from 1:1 line within measurement uncertainties in general. RMSDs and fitting errors $\leq \pm 0.03$ m^{3}m^{-3}, with negligible biases, were obtained for all the data together

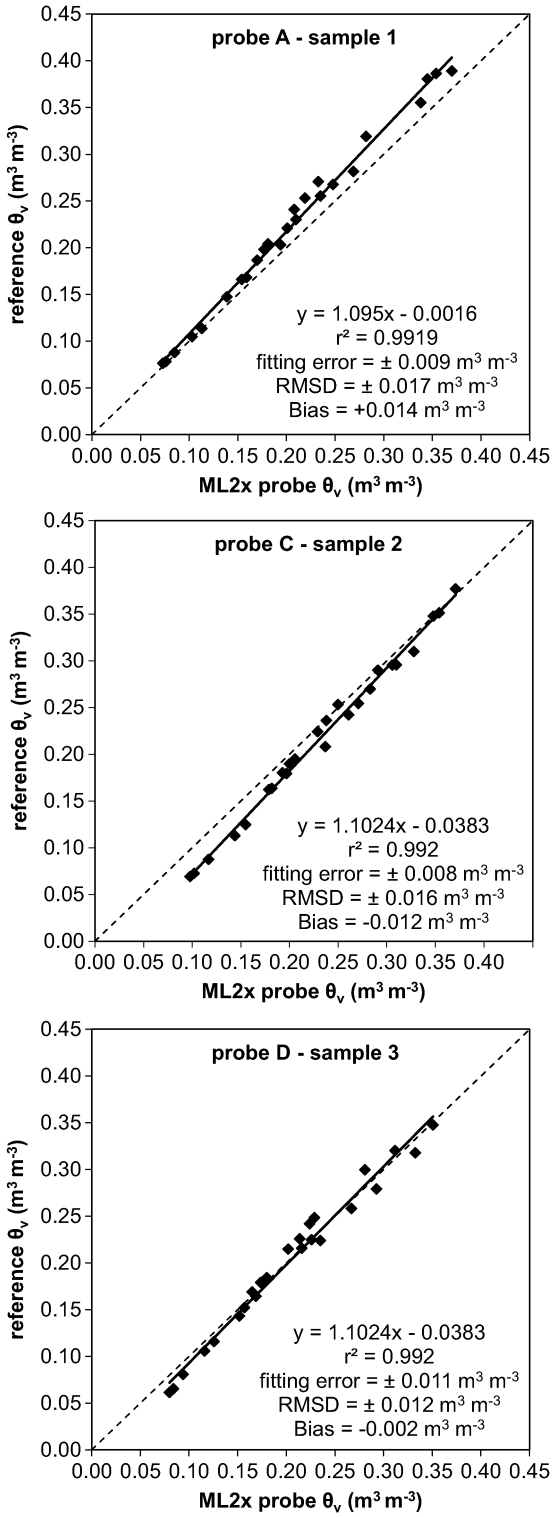

Fig. 3. Examples of the laboratory calibration procedures carried out for the ML2x probes using as reference SM measurements carried out with the gravimetric method (see text). A, C, and D probes are three of the ML2x probes used during the campaign, and samples 1–3 were collected in some of the selected parcels and correspond to loam, clay loam, and silt loam soils, respectively.

and for the different probes separately. It shows the accurate operation of the ML2x probes in field conditions, which provide θ_v with an uncertainty within ± 0.03 m^{3}m^{-3}. Therefore, these

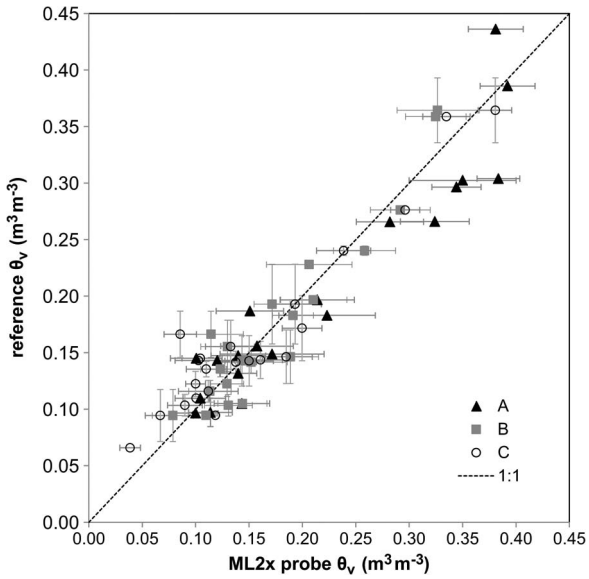

Fig. 4. Test of the ML2x probe operation in the experimental parcels (example for three different ML2x probes, A–C). Reference θ_v values obtained by using the gravimetric method on field-collected samples against concurrent averages of transect data in all the experimental parcels described in Table II.

results validate the manufacturer calibrations for the soils in the experimental sites.

B. Permanent SM Stations

The permanent stations located in the study region measure SM data with Stevens Hydra Probe II probes [24], [27], which have been also widely used for research (http://ismn.geo.tuwien.ac.at/). The CONAE permanent stations contribute with SM Cal/Val activities to the NASA's SM Active Passive (SMAP) mission since CONAE is a SMAP Cal/Val Partner. Data measured at the surface (within the first 5-cm soil depth) by five stations located in the SN node were used in this paper since the SN node is the one with most stations inside. Table III shows station locations and soil textural classes and crop types in the parcels where they are located, which have a minimum size of 0.7×0.7 km^2 and are spatially homogeneous. The Hydra Probe II has a θ_v uncertainty of ± 0.03 m^{3}m^{-3} according to the manufacturer [24], [28]. The manufacturer recommends the use of a linear relationship between θ_v and the square root of the real dielectric constant with specific calibration coefficients for loam soils, which is appropriate for loam, silt loam, clay loam, silty clay loam, sandy clay loam, sandy loam, and some medium textured clay soil samples. This relationship is used to obtain θ_v from the station probe data since it is suitable for all the textural classes present in the study region. Additionally, the Hydra Probe II performance was evaluated by using the gravimetric method, as described earlier, to obtain reference θ_v values in the parcels where the stations are located in field conditions. Linear correlations were obtained between reference and probe θ_v data for each individual parcel (in the range from 0.05 m^{3}m^{-3} to 0.4 m^{3}m^{-3}), with r^2 of about 0.83 and fitting errors and RMSDs of ± 0.03 m^{3}m^{-3}, in agreement with the uncertainty given by the manufacturer.

TABLE III
LOCATIONS, SOIL TEXTURAL CLASSES, AND CROP TYPES FOR THE PERMANENT STATIONS IN THE SN NODE

Station	Geographic latitude	Geographic longitude	Crop type	Soil textural class	(Clay,Silt, Sand) (%)
S1	32º 58' 15.4"S	62º 29' 48.5"W	Soybean	Loam	(25,49,26)
S2	33º 0' 32.3"S	62º 29' 17.1"W	Soybean	Loam	(21,47,32)
S3	32º 58' 31.8"S	62º 27' 31.9"W	Soybean	Loam	(26,43,31)
S4	32º 58' 20.3"S	62º 27' 5.1"W	Soybean	Clay loam	(29,45,26)
S5	32º 58' 22.7"S	62º 29' 57.0"W	Maize	Loam	(24,48,28)

C. SMOS and Ground Data Comparison Methodology

Volumetric SM content θ_v values were extracted from concurrent SMOS MIR_SMUDP2 products (v5.51) for the four experimental nodes throughout the field campaign duration, i.e., February, 2013 (see Table I). Additionally, values of the data quality index (DQX), which includes an estimate of the theoretically retrieved standard deviation [5], were also extracted for the SMOS-retrieved θ_v data. RFI probabilities were much lower than 10% for all the cases ($\leq$0.015). Average values and standard deviations of all the handheld θ_v measurements collected in each node during the campaign (i.e., using the measurements taken by each probe along transects in the different parcels within the node) were assessed to be compared with the SMOS MIR_SMUDP2 θ_v data. The uncertainty assigned to the average values per node of the handheld measurements involves the calibration uncertainty of the ML2x probes (see Section II-A) and the variability of the measurements per node for each SMOS overpass.

During the campaign, handheld measurements along transects were carried out in the parcels where SM stations were permanently located, mainly in those within the SN node. The comparison of station data with averages of transect measurements at the station parcels show an average θ_v difference of -0.003 m^{3}m^{-3}, with a standard deviation of the differences of ± 0.03 m^{3}m^{-3}. This comparison results show the station SM data reliability as a parcel measurement. However, these measurements were also used to check the validity of the data provided by the stations in a given node to give an SM value representative of the whole node. The objective was to use node representative data obtained from station data series as ground reference to evaluate the SMOS SM product beyond the field campaign term. Since the SN node have five stations inside, unlike the other nodes (see Fig. 1), a comparison between the average of the transect data measured in the different parcels within this node and the average of the θ_v data provided by the five stations (four in soybean parcels and one in a maize parcel, as shown in Table III) was performed to analyze the station data representativeness at node scale. Station data are acquired at hourly intervals, and they were temporally interpolated (with a cubic spline method) to the handheld measurement times. The mean bias of the differences between node average handheld and station measured θ_v was negligible, -0.002 m^{3}m^{-3}, with a standard deviation of ± 0.02 m^{3}m^{-3}. A good correlation was obtained between both data, with $r^2 = 0.98$ and a linear regression fitting error of ± 0.010 m^{3}m^{-3}. The data agreement points out that the mean data of the stations located inside the SN node can be considered representative θ_v data for the node to evaluate the SMOS MIR_SMUDP2 product over a longer period. Section III-B shows the evaluation of the product when comparing with mean station data acquired in the SN node from June 2012 to December 2014.

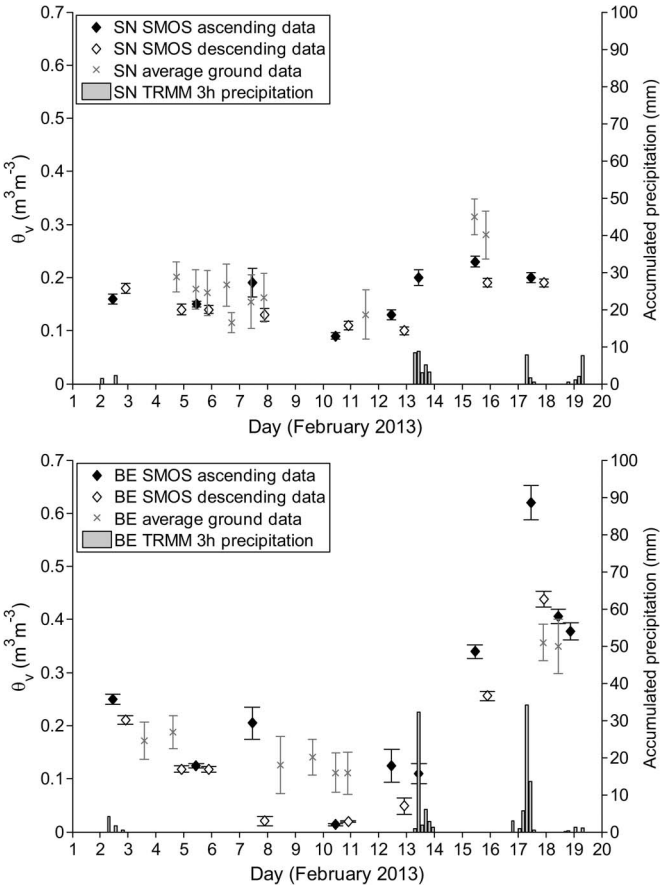

Fig. 5. Time series of the SMOS-retrieved θ_v data and average values of all the handheld measurements acquired within the two nodes with the majority of data collected during the campaign (i.e., SN and BE nodes). Data acquired in both SMOS ascending (10:30–11:00 UTC) and descending (21:30–22:00 UTC) overpasses are shown as solid and empty diamonds, respectively. TRMM 3-h accumulated precipitation data are shown in the secondary axis.

III. RESULTS AND DISCUSSION

A. Evaluation With Handheld Measurements

Fig. 5 shows the evolution of the SMOS-retrieved θ_v data together with the average values per node of the handheld measurements at nodes SN and BE, for which the majority of ground measurements were taken during the field campaign (see Table I). SMOS data error bars show the MIR_SMUDP2 product DQX values, and error bars for node average ground data show the measurement uncertainty assessed, as described

in Section II-C. Fig. 5 shows an overall correlation in the temporal evolution of the time series for node average ground data and SMOS-retrieved data for both nodes. Handheld θ_v measurements taken at these nodes even with no concurrent SMOS overpasses are also included in Fig. 5 to monitor the θ_v temporal evolution. Some sampling days with and without SMOS overpasses, such as those on day 12 (see Table I), were measured at the other nodes. SMOS-retrieved data for the SN and BE nodes were very similar early in the month, as was expected considering the proximity of the nodes ($\sim$60 km) and the similarity with respect to vegetation and soil types (dominated by soybean crops and loam soils). Then, the SMOS values for the BE node dropped to near-zero values at the end of day 7 and during day 10 (both at ascending and descending overpass time). Further in the month, θ_v increased for both nodes starting around day 13, with BE once more displaying substantial variability as SMOS-retrieved θ_v peaked at an extreme value of 0.62 m^3m^{-3}, after which the values decreased to around 0.4 m^3m^{-3}. The difference between the data for the nodes demonstrated the variability of SMOS values over similar regions, mainly due to local meteorological differences. Fig. 5 also shows 3-h and $0.25^\circ \times 0.25^\circ$ accumulated precipitation data provided by the Tropical Rainfall Measuring Mission (TRMM), TRMM_3B42.007 product [29], for the SN and BE node locations. Despite the relatively coarse spatial resolution, these data show differences in the accumulated precipitations for the two nodes. Rain events were registered on the 13th from midday, on the 16th evening, and on the 17th. Rain events showed higher intensity for the BE node, with the 16th–17th event explaining the extreme SMOS value for this node.

In general, SMOS seems to underestimate ground data for both nodes. However, following the SMOS θ_v peak at the BE node, ground values are lower than SMOS data. When rain occurs, it wets the layer from the surface, and a thin saturated soil layer can result in a contributing depth that is shallower than 5 cm [6], [8]. In this case, the reduction of the contributing depth results in overestimating handheld measurements collected from 0 to 5 cm. Following a rainfall event, the SM within the surface soil layer will equilibrate through drainage and hydraulic redistribution. The time required to reach this state depends on the antecedent conditions, the intensity of precipitation, and the soil hydraulic properties [8]. Therefore, the rainfall events on the 16th–17th could explain the SMOS overestimation for the two last ground data at the BE node. However, this is not the case for the two last ground data at the SN node, where an SMOS underestimation is still observed after the rainfall event on the 13th, probably due to the lower accumulated precipitation in this area.

The effect of the different crop types within a node was investigated by comparing parcel average ground θ_v values, i.e., the averages of the handheld measurements taken in each individual parcel, within the SN node. Fig. 6 shows the evolution of the parcel θ_v averages for the different parcels in the SN node, with the dotted lines corresponding to parcels containing maize and the solid lines to soybean crops. The data associated with maize crops do not noticeably deviate in comparison to soybean crops, implying that they do not have a major effect on the node values. The same conclusion was drawn from data

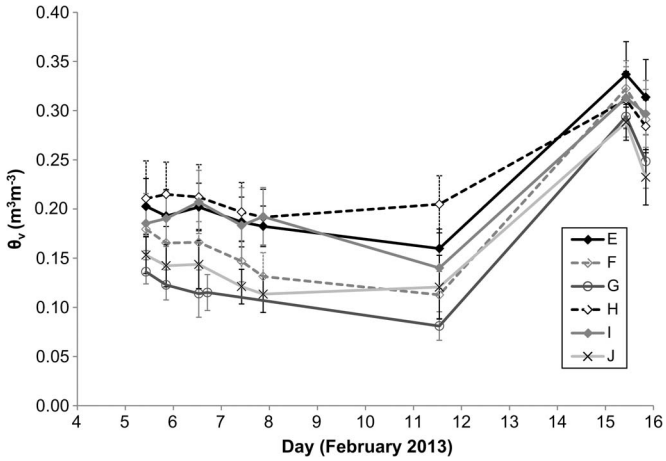

Fig. 6. Average θ_v of the handheld measurements taken along transects in the different parcels (called E–J) within the SN node (details in Table II). Dotted and solid lines for maize and soybean parcels, respectively.

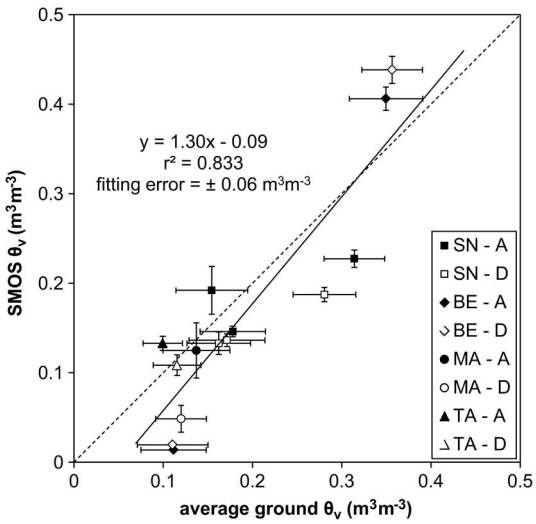

Fig. 7. SMOS-retrieved θ_v data against average θ_v values of all the handheld measurements acquired within a node concurrently with each SMOS overpass during the campaign. Data are plotted per node and for SMOS ascending (solid symbols) and descending (empty symbols) overpasses separately.

of the other nodes. There was no trend observed with parcel crop. Neither there was any general trend with soil type, maybe due to the similarity of parcel textural classes (see Table II). A noticeable feature of Fig. 6 is the negative correlation between θ_v and the spread of measured values. The values across parcels are most similar for the large θ_v at day 15 (with a mean θ_v of 0.311 m^3m^{-3} and a standard deviation of ± 0.018 m^3m^{-3} for all the parcels), whereas the spread of values for drier soils, e.g., at day 11, is substantially larger (with a mean θ_v of 0.14 m^3m^{-3} and a standard deviation of ± 0.04 m^3m^{-3} for all the parcels), which is apparently not crop related. In any case, the variability among parcels was taken into account in the estimation of the node ground θ_v uncertainties (see Section II-C), shown as error bars in Fig. 5.

Fig. 7 shows the correlation between SMOS-retrieved data and the concurrent node average ground values for the four experimental nodes and SMOS ascending (solid symbols) and

descending (empty symbols) overpasses, with the dotted line representing the 1:1 relationship. A linear fit of all the data is shown as a solid line, which equation has a relatively high coefficient of determination (r^2) of 0.83 and a fitting error of ± 0.06 m^{3}m^{-3}. Fig. 7 seems to show a tendency of the SMOS data to underestimate θ_v values for soils with low to moderate θ_v, and to slightly overestimate values for soils with high θ_v, although this will be further discussed with a larger data set in Section III-B. This figure also reflects larger amplitude of SMOS data compared with ground measurements, which is in part explained by the aforementioned possible differences in contributing depth between SMOS-retrieved and ground data. The following linear equation is obtained when data are inversely plotted, i.e., node average ground θ_v as a function of SMOS-retrieved θ_v: $\theta_v = a \cdot \theta_{v,\mathrm{SMOS}} + b$, with $a = 0.66 \pm 0.10$, $b = 0.08 \pm 0.02$ m^{3}m^{-3}, and a fitting error of ± 0.04 m^{3}m^{-3}. From all the data, a bias (i.e., the average difference between the SMOS-retrieved and node average ground measured θ_v data) of -0.02 m^{3}m^{-3} is obtained, showing how the majority of SMOS-retrieved values underestimate ground measurements. The standard deviation of the differences is ± 0.06 m^{3}m^{-3}, obtaining an RMSD of ± 0.06 m^{3}m^{-3}. These results are in agreement with those obtained in [4], [12], and [13], and much better than those in [10] and [11]. The differences observed between our results and those in previous studies can be a consequence of several factors, such as the improvement offered by the latest version of the SMOS MIR_SMUDP2 product (v5.51), the level of RFIs (our experimental sites are hardly affected, unlike, e.g., the study region in [10]), the measurement quality and representativeness at the SMOS spatial resolution (since the study region is a quite homogeneous rain-fed and flat cropland area that enables it), and the good quality of auxiliary data files such as ECOCLIMAP land cover and FAO soil properties in the region. All these factors make the study area a suitable site to evaluate the performance of the SMOS SM retrieval algorithm in itself, as uncertainties originating from external factors are minimized. Differences between the SMOS-retrieved and node average ground measured θ_v data of -0.01 ± 0.06 m^{3}m^{-3} and -0.04 ± 0.06 m^{3}m^{-3} are obtained separately for the data acquired by SMOS ascending (50% of events) and descending overpasses, which lead to similar RMSDs of ± 0.06 and ± 0.07 m^{3}m^{-3}, respectively.

B. Evaluation With Permanent SM Station Data

SMOS-retrieved θ_v data, both acquired with the SMOS ascending and descending overpasses, were also compared with station mean θ_v values for the SN node for two and a half years of available station data (from June 2012 to December 2014) (see Fig. 8). SMOS data with DQX > 0.03 m^{3}m^{-3} were filtered out for the study (still remaining the 97.5% of the data, with a mean DQX value of 0.007 ± 0.004 m^{3}m^{-3} for the whole period). RFI probabilities were ≤ 0.015, both for SMOS ascending and descending overpass data. Fig. 8 shows a general underestimate by the SMOS product, both for ascending and descending overpasses, without significant differences. Similar r^2 values were obtained in both cases, with values of 0.644 and 0.653 for ascending and descending data, respectively. The following linear equation was obtained when data were inversely plotted, i.e., fitting reference station mean θ_v as a function of SMOS-retrieved θ_v (for ascending and descending overpasses altogether): $\theta_v = a \cdot \theta_{v,\mathrm{SMOS}} + b$, with $a = 0.695 \pm 0.019$, $b = 0.117 \pm 0.004$ m^{3}m^{-3}, $r^2 = 0.636$ and a fitting error of ± 0.04 m^{3}m^{-3}. This expression can be used to adjust the MIR_SMUDP2 v5.51 product data for the study region.

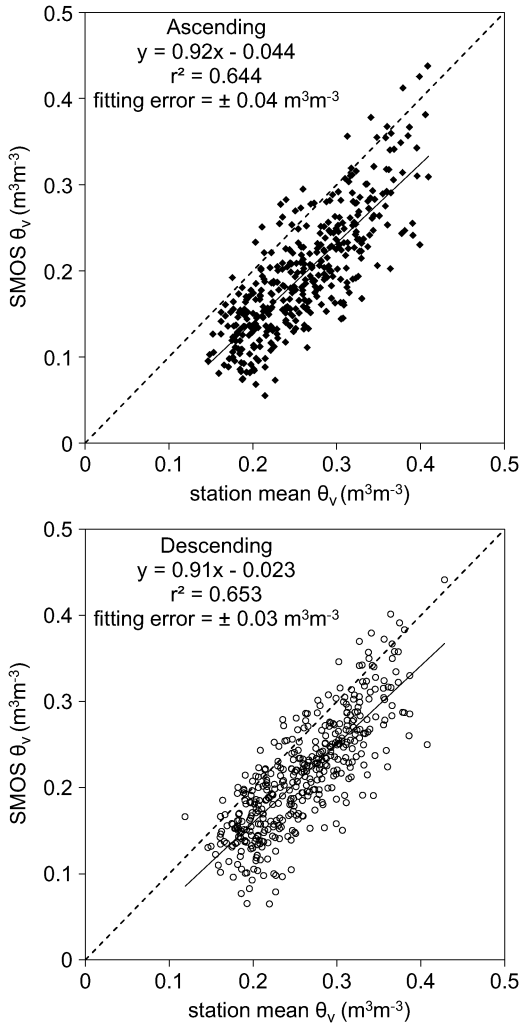

Fig. 8. SMOS-retrieved θ_v against station mean θ_v at the SN node for the whole study period (June 2012–December 2014). SMOS data in ascending and descending overpasses are shown as solid diamonds and empty circles, respectively. Linear regression equations are shown together (see statistical results in Table IV).

Table IV shows statistics for the differences between SMOS-retrieved data and station mean θ_v values for the SN node (June 2012–December 2014). The statistics include: number of cases (N), mean bias (mean), standard deviation (SD), root-mean-square difference (RMSD), median bias (Me), robust standard deviation (RSD), i.e., $\mathrm{RSD} = \mathrm{Me}(|x_i - \mathrm{Me}(x_i)|) * 1.4826$, where $x =$ SMOS θ_v—mean station θ_v [30], robust RMSD (R-RMSD), i.e., $\text{R-RMSD} = (\mathrm{Me}^2 + \mathrm{RSD}^2)^{1/2}$, minimum (min), maximum (max), skewness, kurtosis, and coefficient of determination (r^2). Me and RSD minimize the influence of possible

TABLE IV
DIFFERENCES BETWEEN SMOS-RETRIEVED DATA AND STATION MEAN θ_v VALUES (IN m^3m^{-3}) FOR THE SN NODE AND THE WHOLE STUDY PERIOD (JUNE 2012–DECEMBER 2014). THE STATISTICS INCLUDE: NUMBER OF CASES (N), MEAN BIAS (MEAN), STANDARD DEVIATION (SD), RMSD ($\text{RMSD} = (\text{mean}^2 + \text{SD}^2)^{1/2}$) MEDIAN BIAS (ME), AND ROBUST STANDARD DEVIATION (RSD, $\text{RSD} = \text{Me}(|x_i - \text{Me}(x_i)|) * 1.4826$, WHERE x = SMOS θ_v—MEAN STATION θ_v), ROBUST RMSD(R-RMSD $= (\text{Me}^2 + \text{RSD}^2)^{1/2}$), MINIMUM (MIN), MAXIMUM (MAX), SKEWNESS, KURTOSIS, AND COEFFICIENT OF DETERMINATION (r^2). RESULTS FOR SMOS DATA ACQUIRED IN ASCENDING AND DESCENDING OVERPASSES ARE ALSO ANALYZED SEPARATELY

	All	Ascending	Descending
N	806	383	423
mean	-0.05	-0.06	-0.05
SD	0.04	0.04	0.04
RMSD	0.07	0.08	0.06
Me	**-0.05**	**-0.07**	**-0.04**
RSD	**0.04**	**0.04**	**0.04**
R-RMSD	**0.07**	**0.08**	**0.06**
Min	-0.19	-0.19	-0.16
Max	0.06	0.06	0.05
Skewness	-0.10	0.11	-0.20
Kurtosis	-0.17	-0.07	0.03
r^2	0.64	0.64	0.65

outliers and can be considered statistically more consistent validation parameters than mean and SD [31], although the similarity between mean and median and between SD and RSD denotes a small effect of outliers in this case. Skewness and kurtosis quantitatively describe the distribution of the differences between SN-node SMOS-retrieved θ_v and station mean θ_v and explain the small discrepancies between mean and median and SD and RSD. The distributions passed successfully a Kolmogorov–Smirnov test with the Lilliefors significance correction and a Shapiro–Wilk test [32], [33], which means that they fit to a normal distribution, and the statistics used describes properly the evaluation results. A Me of -0.05 m^3m^{-3}, which means a SMOS general underestimation, and an RSD of ± 0.04 m^3m^{-3} are finally obtained from the differences between the SMOS-retrieved data and station mean θ_v values for all the concurrent data over the study period, with a R-RMSD of ± 0.07 m^3m^{-3}. The R-RMSD, as a quadratic sum of systematic and random errors, gives an estimate of the SMOS product agreement with the reference station data and can be considered the product accuracy at the study region.

Table IV also includes the statistics when results are separated for SMOS ascending and descending overpasses. Me values of -0.07 and -0.04 m^3m^{-3} are obtained for data in ascending and descending overpasses, respectively, with RSDs of ± 0.04 m^3m^{-3}. Although the implied R-RMSDs in SMOS-retrieved data (of ± 0.08 m^3m^{-3} and ± 0.06 m^3m^{-3} for ascending and descending overpasses, respectively) are higher than the SMOS mission's goal of ± 0.04 m^3m^{-3}, these results show relatively high accuracy for the MIR_SMUDP2 product. It should be noted that the negative biases observed (i.e., systematic errors) increase the R-RMSDs above the mission's goal since the random errors (estimated with the RSDs) equal this goal, such as in [13].

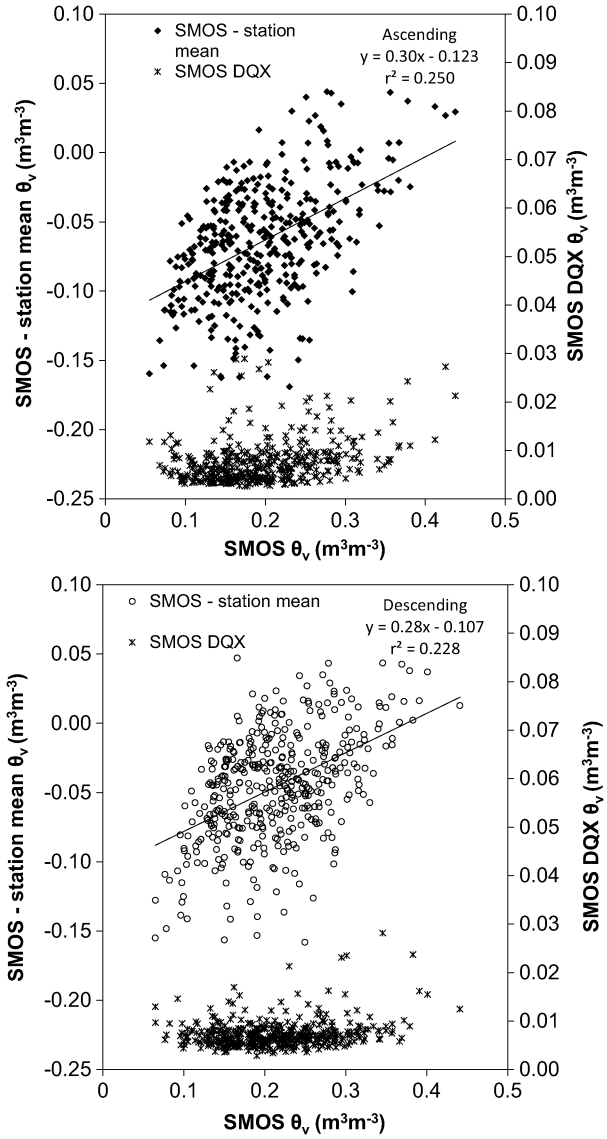

Fig. 9. SMOS-station mean θ_v differences at the SN node against SMOS-retrieved θ_v data are shown in the primary axis, together with the SMOS θ_v uncertainties, shown as DQX in the MIR_SMUDP2 product, in the secondary axis (crosses). SMOS data in both ascending (solid diamonds) and descending (empty circles) overpasses are shown separately.

Fig. 9 shows the SMOS—mean station θ_v differences against SMOS-retrieved θ_v data for the SN node and for ascending and descending overpasses separately, together with the SMOS θ_v uncertainties, shown as DQX in the MIR_SMUDP2 product, in a secondary axis. A clear tendency for the differences to decrease in absolute value with increasing SMOS θ_v values is observed, i.e., the differences are larger for lower SMOS θ_v values, but the same pattern is not encountered in the case of SMOS DQX θ_v uncertainties. As mentioned earlier, DQX θ_v uncertainties are calculated during the product retrieval process based on known error sources, such as the radiometric accuracy of the SMOS acquired brightness temperatures, and their propagation through the modeling process. Possible

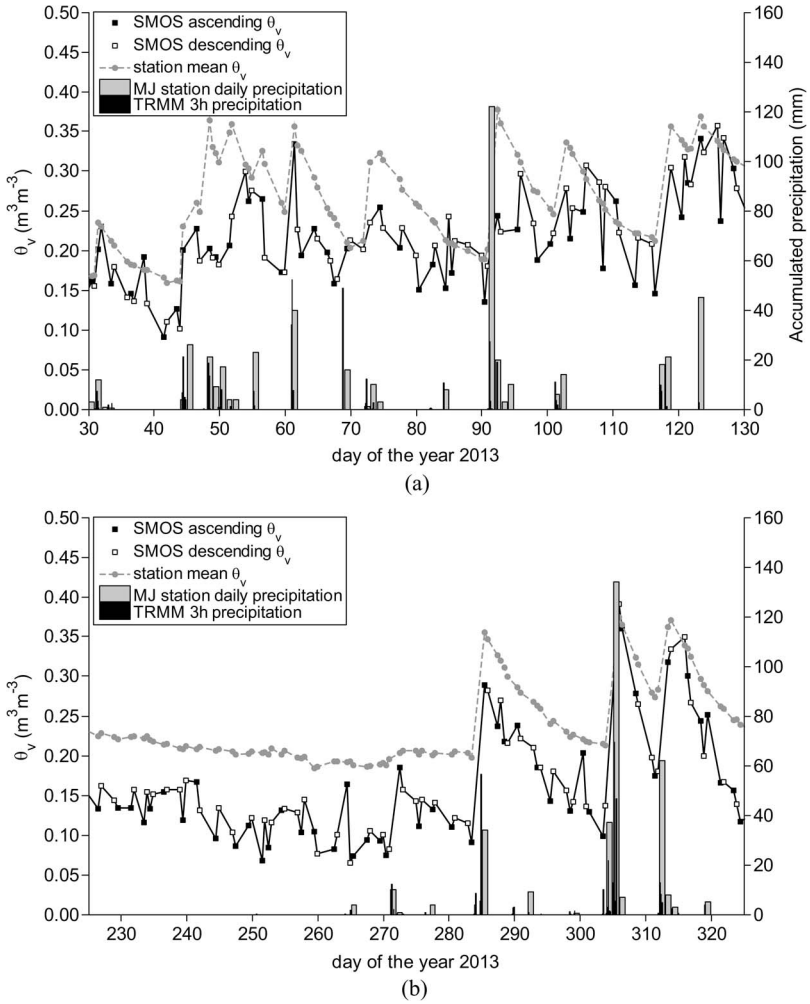

Fig. 10. Comparison of the SMOS-retrieved θ_v data, in both ascending (solid squares) and descending (empty squares) overpasses, and concurrent station mean θ_v data for the SN node, together with accumulated precipitation data from a near WMO station called Marcos Juarez (daily) and TRMM data (3-hourly and $0.25^\circ \times 0.25^\circ$), over two periods of 2013. (a) Days 30–130 (summer) and (b) 225–325 (winter–spring).

SMOS users should be aware of the observed tendency in such surface conditions, with a larger SMOS underestimation for lower SMOS values, since it is not reflected in the estimate of the uncertainty included in the DQX data.

Fig. 10 shows, as an example, a comparison of the SMOS-retrieved and station mean θ_v data for the SN node, together with precipitation data, over two periods of 2013. The precipitation was obtained from two sources: (a) daily accumulated precipitation from the *Marcos Juarez* station (station number 87467, 32°42′S, 62°09′W, 45 km from the SN node center) included in the World Meteorological Organization (WMO) World Weather Watch Program according to WMO Resolution 40 and provided by the NOAA National Climatic Data Center (NOAA-NCDC) (http://www7.ncdc.noaa.gov/CDO/cdoselect.cmd), and (b) 3-h and $0.25^\circ \times 0.25^\circ$ accumulated precipitation from the aforementioned TRMM_3B42.007 product, which data covers spatially the SN node. Fig. 10 shows that SMOS reproduces the θ_v temporal evolution reasonably well and SMOS θ_v generally increases after significant precipitation events [e.g., see days 285, 305, and 312 in Fig. 10(b)], although in some cases, the difference between station mean and SMOS θ_v data seems to increase after them [e.g., see days 47 and 91 in Fig. 10(a)]. The largest range of SMOS-station mean θ_v differences are observed after precipitation events, obtaining differences from -0.20 to $+0.05$ $\mathrm{m^3m^{-3}}$. Moreover, Fig. 10(b) shows that SMOS data present a high temporal variability even in periods without significant precipitation events, e.g., in days 225–285, when only the SMOS peak after the low precipitation event in day 272 (not reproduced by the station data) could be correlated with rainfall. During this period, the SD of SMOS θ_v is ± 0.03 $\mathrm{m^3m^{-3}}$ for ascending and descending overpass data altogether, with a difference between the maximum and the minimum (max-min) of 0.12 $\mathrm{m^3m^{-3}}$, whereas an SD of ± 0.011 $\mathrm{m^3m^{-3}}$ and a max-min of 0.04 $\mathrm{m^3m^{-3}}$ were obtained for the station mean θ_v data. When SMOS data is separated into ascending and descending overpasses, SDs of ± 0.03 $\mathrm{m^3m^{-3}}$ are obtained in both cases during this period, with max-min differences of ± 0.12 and ± 0.10 $\mathrm{m^3m^{-3}}$, respectively. In general, the higher temporal variability of the SMOS product compared with ground measurements (see also Figs. 7 and 8) can be consequence of the soil contributing depth sensitivity of the

SMOS radiometric measurements to skin surface [6] (being much shallower than 5 cm after heavy rainfalls), whereas station probe measurement depth is constant (at the soil top 5 cm). Additionally, the drying process after important rainfalls could be faster for SMOS data than for station data due to different contributing depths. However, these are not likely the reasons of the temporal variability observed in periods without precipitation events (days 225–285), which should be better investigated, e.g., by analyzing technical issues with SMOS instrumentation [17] or possible leftover artifacts in the retrieval algorithm.

IV. Summary and Conclusion

An experimental campaign was carried out in the PRA in February 2013 with the aim of evaluating the latest operational version of the SMOS MIR_SMUDP2 product (v5.51) in rainfed croplands, due to the importance of monitoring SM in such land covers to improve crop yield estimation and to evaluate water balance. Several papers have been devoted to assess the accuracy of the MIR_SMUDP2 product (mostly for previous versions) over different regions, but this is the first time this is addressed in South America, where the RFI contamination is really weak in both ascending and descending overpasses, unlike in other validation sites used around the world [10], [17], which makes the region optimal to study differences in the SMOS retrievals from both orbits. Additionally, the area is well suited to study the operation of the SMOS SM retrieval algorithm in itself, as uncertainties originating from external factors, e.g., topography, heterogeneities, vegetation effects, RFI contamination, poor quality in the auxiliary data, and soil property effects, are minimized.

The comparison of concurrent MIR_SMUDP2 data (acquired in both ascending and descending overpasses) with average values of handheld measurements taken along transects over representative parcels within four SMOS DGG nodes during a one-month field campaign showed a slight θ_v underestimation by the SMOS product of -0.02 m^{3}m^{-3} and an RMSD of ± 0.06 m^{3}m^{-3}.

The good agreement obtained between averages of the handheld θ_v measurements within the SN node and concurrent averages of the data acquired by five permanent stations within this same node, i.e., with a negligible bias and a standard deviation ± 0.02 m^{3}m^{-3}, suggested the possibility of using temporal series of the SN node mean station data to extend the SMOS product evaluation beyond the campaign period. A comparison of the MIR_SMUDP2 data with station mean θ_v values for the SN node over two and a half years (June 2012–December 2014) showed again a SMOS product general underestimation of -0.05 m^{3}m^{-3} and an R-RMSD of ± 0.07 m^{3}m^{-3} (± 0.08 m^{3}m^{-3} and ± 0.06 m^{3}m^{-3} for SMOS data in ascending and descending overpasses, separately).

Although it might be expected that SM has better performance for SMOS ascending data [8], [17], due to smaller SM and temperature gradients within the contributing depth, our results do not confirm this. No significant differences were found between the use of data acquired in ascending and descending orbits in our study region, such as in [8], and [13], and in contrast to the results shown by Rowlandson *et al.* [17] over the Midwest United States, where RFI contamination for ascending orbits could influence the SMOS brightness temperatures and the SM product results.

A tendency for the SMOS-station mean θ_v differences to decrease in absolute values with increasing SMOS θ_v values was observed. Moreover, even in periods without precipitation events, a significant SMOS θ_v temporal variability (i.e., much larger than the SMOS θ_v uncertainty provided as DQX) was shown, which was not reproduced by the station data.

The MIR_SMUDP2 θ_v accuracy observed in the study region, when using both the handheld measurements and the station data as reference data for its evaluation, is relatively lower than the mission's accuracy goal of ± 0.04 m^{3}m^{-3}, due to the significant dry bias observed (i.e., negative systematic error), since standard deviation (i.e., random error) equal this goal. Therefore, a general underestimation is observed for the SMOS product, which was also observed in other regions of the world for previous product versions (e.g., in [4] and [11]–[13]), but despite this underestimation, SMOS seems able to monitor the temporal evolution of ground SM data in this area of rainfed croplands.

Acknowledgment

The authors would like to thank CONAE for providing the permanent SM station data and the Instituto de Hidrología de Llanuras (IHLLA, UNCPBA, CIC, MA) for the logistic support during and after the experimental campaign. The SMOS data were provided by ESA under Cat-1 Project AO 4748.

References

[1] Y. H. Kerr *et al.*, "The SMOS mission: New tool for monitoring key elements of the global water cycle," *Proc. IEEE*, vol. 98, no. 5, pp. 666–687, May 2010.

[2] S. Mecklenburg *et al.*, "ESA's soil moisture and ocean salinity mission: Mission performance and operations," *IEEE Trans. Geosci. Remote Sens.*, vol. 50, no. 5, pp. 1354–1366, May 2012.

[3] Y. H. Kerr *et al.*, "The SMOS soil moisture retrieval algorithm," *IEEE Trans. Geosci. Remote Sens.*, vol. 50, no. 5, pp. 1384–1403, May 2012.

[4] J. P. Wigneron *et al.*, "First evaluation of the simultaneous SMOS and ELBARA-II observations in the Mediterranean region," *Remote Sens. Environ.*, vol. 124, pp. 26–37, Sep. 2012.

[5] CESBIO, IPSL-Service d'Aéronomie, INRA-EPHYSE, Reading University, Tor Vergata University, "Algorithm Theoretical Basis Document (ATBD) for the SMOS Level 2 soil moisture processor," Array Syst. Comput. Inc., Toronto, ON, Canada, SO-TN-ARR-L2PP-0037, no. 3.5, Jul. 28, 2011.

[6] M. J. Escorihuela, A. Chanzy, J. P. Wigneron, and Y. Kerr, "Effective soil moisture sampling depth of L-band radiometry: A case study," *Remote Sens. Environ.*, vol. 114, no. 5, pp. 995–1001, May 2010.

[7] O. Merlin *et al.*, "Disaggregation of SMOS soil moisture in Southeastern Australia," *IEEE Trans. Geosci. Remote Sens.*, vol. 50, no. 5, pp. 1556–1571, May 2012.

[8] T. J. Jackson *et al.*, "Validation of Soil Moisture and Ocean Salinity (SMOS) soil moisture over watershed networks in the U.S.," *IEEE Trans. Geosci. Remote Sens.*, vol. 50, no. 5, pp. 1530–1543, May 2012.

[9] J. P. Wigneron *et al.*, "L-band Microwave Emission of the Biosphere (L-MEB) model: Description and calibration against experimental data sets over crop fields," *Remote Sens. Environ.*, vol. 107, no. 4, pp. 639–655, Apr. 2007.

[10] J. T. Dall'Amico, F. Schlenz, A. Loew, and W. Mauser, "First results of SMOS soil moisture validation in the upper danube catchment," *IEEE Trans. Geosci. Remote Sens.*, vol. 50, no. 5, pp. 1507–1516, May 2012.
[11] I. Gherboudj *et al.*, "Validation of SMOS data over agricultural and boreal forest areas in Canada," *IEEE Trans. Geosci. Remote Sens.*, vol. 50, no. 5, pp. 1623–1635, May 2012.
[12] A. Al Bitar *et al.*, "Evaluation of SMOS soil moisture products over continental U.S. using the SCAN/SNOTEL network," *IEEE Trans. Geosci. Remote Sens.*, vol. 50, no. 5, pp. 1572–1586, May 2012.
[13] N. Sánchez, J. Martínez-Fernández, A. Scaini, and C. Pérez-Gutiérrez, "Validation of the SMOS L2 soil moisture data in the REMEDHUS network (Spain)," *IEEE Trans. Geosci. Remote Sens.*, vol. 50, no. 5, pp. 1602–1611, May 2012.
[14] S. Louvet *et al.*, "SMOS soil moisture product evaluation over West-Africa from local to regional scale," *Remote Sens. Environ.*, vol. 156, pp. 383–394, Jan. 2015.
[15] M. E. Holzman, R. Rivas, and M. C. Piccolo, "Estimating soil moisture and the relationship with crop yield using surface temperature and vegetation index," *Int. J. Appl. Earth Observ. Geoinf.*, vol. 28, pp. 181–192, May 2014.
[16] A. Mialon *et al.*, "Comparison of Dobson and Mironov dielectric models in the SMOS soil moisture retrieval algorithm," *IEEE Trans. Geosci. Remote Sens.*, vol. 53, no. 6, pp. 3084–3094, Jun. 2015.
[17] T. L. Rowlandson, B. K. Hornbuckle, L. M. Bramer, J. C. Patton, and S. D. Logsdon, "Comparisons of evening and morning SMOS passes over the Midwest United States," *IEEE Trans. Geosci. Remote Sens.*, vol. 50, no. 5, pp. 1544–1555, May 2012.
[18] A. Mialon, L. Coret, Y. H. Kerr, F. Sécherre, and J.-P. Wigneron, "Flagging the topographic impact on the SMOS signal", *IEEE Trans. Geosci. Remote Sens.*, vol. 46, no. 3, pp. 689–694, Mar. 2008.
[19] O. Arino *et al.*, "GlobCover: The most detailed portrait of Earth," *ESA Bull.*, vol. 136, pp. 24–31, 2008.
[20] Z. Wan and J. Dozier, "A generalized split-window algorithm for retrieving land surface temperature from space," *IEEE Trans. Geosci. Remote Sens.*, vol. 34, no. 4, pp. 892–905, Jul. 1996.
[21] User Manual. ThetaProbe ML2x Soil Moisture Sensor (ML2x-UM-1.21), Delta-T Devices Ltd., Cambridge, U.K., 1999.
[22] A. Malicki, R. Plagge, and C. H. Roth, "Improving the calibration of dielectric TDR soil moisture determination taking into account the solid soil," *Eur. J. Soil Sci.*, vol. 47, no. 3, pp. 357–366, Sep. 1996.
[23] G. C. Topp and W. D. Reynolds, "Time domain reflectometry: A seminal technique for measuring mass and energy in soil," *Soil Tillage Res.*, vol. 47, no. 1/2, pp. 125–132, Jun. 1998.
[24] M. S. Seyfried, L. E. Grant, E. Du, and K. Humes, "Dielectric loss and calibration of the hydra probe soil water sensor," *Vadose Zone J.*, vol. 4, no. 4, pp. 1070–1079, Nov. 2005.
[25] P. R. Day, "Particle fractioning and particle-size analysis," in *Methods of Soil Analysis, Vol. I, Physical and Mineralogical Properties, Including Statistics of Measurement and Sampling, Agronomy*, vol. 9, C. A. Black, Ed. Madison, WI, USA: Amer. Soc. of Agronomy, Inc., 1965 pp. 545–567.
[26] M. Mira, E. Valor, R. Boluda, V. Caselles, and C. Coll, "Influence of soil water content on the thermal infrared emissivity of bare soils: Implication for land surface temperature determination," *J. Geophys. Res.*, vol. 112, no. F4, Dec. 2007, Art. ID. F04003.
[27] M. S. Seyfried and M. D. Murdock, "Measurement of soil water content with a 50-MHz soil dielectric sensor," *Soil Sci. Soc. Amer. J.*, vol. 68, no. 2, pp. 394–403, Mar. 2004.
[28] Comprehensive Stevens Hydra Probe II User's Manual, Stevens Water Monitoring System Inc., Portland, OR, USA, 2007.
[29] G. J. Huffman and D. T. Bolvin, TRMM and Other Data Precipitation Data Set Documentation, 2013, 40pp. [Online]. Available: ftp://meso-a.gsfc.nasa.gov/pub/trmmdocs/3B42_3B43_doc.pdf
[30] P. T. Wilrich, "Robust estimates of the theoretical standard deviation to be used in interlaboratory precision experiments," *Accred. Qual. Assur.*, vol. 12, no. 5, pp. 231–240, May 2007.
[31] P. Schneider, D. Ghent, G. Corlett, F. Prata, and J. Remedios, "AATSR validation: LST Validation Protocol," Univ. Leicester, Leicester, U.K., UL-NILU-ESA-LST-LVP Issue 1 Revision 0, 2012, 39 pp. [Online]. Available: http://lst.nilu.no/Portals/73/Docs/Reports/UL-NILU-ESA-LST-LVP-Issue1-Rev0-1604212.pdf
[32] W. Conover, *Practical Nonparametric Statistics*. New York, NY, USA: Wiley, 1980.
[33] D. J. Steinskog, D. B. Tjøstheim, and N. G. Kvamstø, "A cautionary note on the use of the Kolmogorov-Smirnov test for normality," *Mon. Weather Rev.*, vol. 135, no. 3, pp. 1151–1157, Mar. 2007.

Raquel Niclòs received the B.Sc., M.Sc., and Ph.D. degrees from the University of Valencia, Burjassot, Spain, in 2000, 2002, and 2005, respectively, all in physics.

She currently has a "*Ramón y Cajal*" Research Contract (Spanish National R & D & I Plan) with the Department of Earth Physics and Thermodynamics, Faculty of Physics, University of Valencia. She is the author of 23 papers in SCI international journals and more than 100 other works, such as non-SCI papers, book chapters, and conference proceedings. Her research interests include sea and land remote sensing techniques, mainly related to the determination of surface temperature and thermal infrared emissivity, for environmental and meteorological applications.

Raúl Rivas received the M.S. degree in environmental physics and the Ph.D. degree in physics from the University of Valencia, Valencia, Spain, in 2003 and 2004, respectively.

He is currently an Independent Researcher and a member of the Directorate of Comisión de Investigaciones Científicas, Buenos Aires, Argentina. He is also with the Remote Sensing Group, Instituto de Hidrología de Llanuras. His main research interests include remote sensing and hydrology (more than 20 years of experience), thermal infrared, surface energy balance, and evapotranspiration. His current research interests include monitoring networks for hydrology research.

Vicente García-Santos received the B.Sc., M.Sc., and Ph.D. degrees from the University of Valencia, Burjassot, Spain, in 2007, 2010, and 2013, respectively, all in physics.

He is currently a Postdoctoral Researcher with the Thermal Remote Sensing Group, Department of Earth Physics and Thermodynamics, Faculty of Physics, University of Valencia. He is the author of eight papers published in international journals and 35 conference papers. His research interest include the physical processes of thermal infrared remote sensing with special attention to the retrieval and validation of land surface temperature and emissivity products and characterization and correction of atmospheric effects.

Carolina Doña received the B.Sc. and M.Sc. degrees in physics and remote sensing from the University of Valencia, Burjassot, Spain, in 2008 and 2012, respectively. She is currently working toward the Ph.D. degree in remote sensing with the University of Valencia.

She is with the Thermal Remote Sensing Group, Department of Earth Physics and Thermodynamics, Faculty of Physics, University of Valencia. Her research interests include the water quality and quantity in lenitic environments, and calibration/validation of radiometric data from remote sensing sensors.

Enric Valor received the B.Sc., M.Sc., and Ph.D. degrees in physics from the University of Valencia, Burjassot, Spain, in 1992, 1994, and 1997, respectively.

He is currently an Associate Professor of earth physics with the Department of Earth Physics and Thermodynamics, University of Valencia. He has 20 years expertise in the physical processes involved in temperature measurement using remote sensing techniques, which has been documented through four books, four doctoral theses, 50 papers in international journals, and 70 conference papers. His research interests include the physical processes of thermal infrared remote sensing, emissivity characterization, atmospheric and emissivity corrections, and temperature emissivity separation algorithms.

Dr. Valor received the Norbert Gerbier-MUMM International Award for 2010, conferred by the World Meteorological Organization.

Mauro Holzman received the Ph.D. degree in geography from Universidad Nacional del Sur, Buenos Aires, Argentina, in 2013.

He is currently with Instituto de Hidrología de Llanuras, Buenos Aires. His research interests include Earth observation hydrology, soil moisture and water vegetation condition, drought early warning systems, crop yield, and evapotranspiration. His current research activity is a validation process based on ground measurements from test sites located in Argentine Pampas of Central Argentina.

Martín Bayala received the B.Sc. degree in environmental science from the Universidad Nacional del Centro de la Provincia de Buenos Aires, Buenos Aires, Argentina, in 2006 and the M.Sc. degree in space applications for emergency early warning and response from the Universidad Nacional de Córdoba, Córdoba, Argentina, in 2011.

He is currently working with the Remote Sensing Group, Instituto de Hidrología de Llanuras, Buenos Aires. His research interests include remote sensing evapotranspiration and energy budget estimation, and the development of methodologies of resampling and artificial neural networks to enhance image resolution.

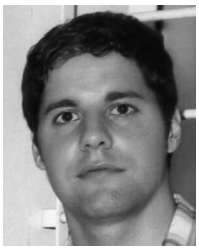

Facundo Carmona was born in Tandil, Argentina, in 1983. He received the B.Sc. degree in environmental technology from the Universidad Nacional del Centro de la provincia de Buenos Aires, Tandil, Argentina, in 2009 and the M.Sc. and Ph.D. degrees in remote sensing from the University of Valencia, Burjassot, Spain, in 2012 and 2014, respectively.

He is currently working as a Consejo Nacional de Investigaciones Científicas y Técnicas (CONICET) Postdoctoral Researcher with the Instituto de Hidrología de Llanuras, Buenos Aires, Argentina. His research interests include remote sensing techniques and hydrology, and the development of new methodologies and/or approaches to the determination of net radiation and evapotranspiration with remote sensing data.

Dora Ocampo was born in Tandil, Argentina, in 1981. She is currently working toward the Ph.D. degree in applied sciences from the University of Luján, Buenos Aires, Argentina.

She conducts research with the Remote Sensing Group, Instituto de Hidrología de Llanuras, Buenos Aires. She has seven years of expertise in the operation and management of weather and energy balance stations. Her research interests include the study of the energy balance and evapotranspiration at different surfaces.

Álvaro Soldano received the B.Eng. degree from the National University of Buenos Aires, Buenos Aires, Argentina, in 2000.

From 1983 to 2009, he worked as a Researcher at the National Water Institute (INA) of Argentina as the Head of the area of remote sensing and geographic information system in the hydrological warning system of Del Plata Basin. Since 2003, he has been a Project Manager in 14 activations of the International Charter: Space and Major Disasters. In 2007, he was a Specialist in remote sensing and geographic information systems applied to the study of the environment from National University of Luján, Buenos Aires. Since 2009, he has been a Researcher from the Argentina Space Agency (CONAE), Buenos Aires, Argentina. Since 2010, he has been coordinating the *in situ* sampling and the field campaigns of the SAOCOM Satellite Mission by CONAE.

Marc Thibeault received the B.Sc. degree in physics from Laval University, Québec, QC, Canada, in 1982; the B.Sc. degree in mathematics from the University of Montreal, Montreal, QC, in 1988; and the D.Sc. degree from the University of Buenos Aires, Buenos Aires, Argentina, in 2004.

He is currently the Strategic Applications Coordinator for the SAOCOM project, a new L-Band mission of Comisión Nacional de Actividades Espaciales, Buenos Aires. His research interests include soil moisture, polarimetry, and other synthetic aperture radar applications.

Vicente Caselles received the B.Sc., M.Sc., and Ph.D. degrees from the University of Valencia, Burjassot, Spain, in 1979, 1980, and 1983, respectively, all in physics.

He is currently a Professor in Earth physics and the Head of the Thermal Remote Sensing Group, Department of Earth Physics and Thermodynamics, University of Valencia. He has 35-year expertise in the physical processes involved in both temperature measurement and evapotranspiration using remote sensing techniques, which has been documented through 10 books, 20 doctoral theses, 100 papers in international journals, and 60 conference papers. He was collaborating with the European Space Agency as a member of the Advisory Group for the Land-Surface Processes and Interactions Mission.

Dr. Caselles served as the Chair of the Spanish Remote Sensing Society and as the Manager of Human Resources and Mobility General Direction, Spanish Ministry of Economy and Competitiveness. He received the Nobert Gerbier-MUMM Internatinal Award 2010 by the World Meteorological Organization.

Juan M. Sánchez received the B.Sc., M.Sc., and Ph.D. degrees from the University of Valencia, Valencia, Spain, in 2003, 2005, and 2008, respectively, all in physics.

He is currently a Lecturer with the Department of Applied Physics, University of Castilla-La Mancha, Almadén, Spain. He is the author of 25 papers published in international journals, five book chapters, and more than 60 conference papers. He has participated in 20 national and international projects, and he is referee in 17 international journals. His research interests include thermal infrared remote sensing in general and the surface energy flux retrieval in particular.

Dr. Sánchez received the Nobert Gerbier-MUMM Internatinal Award 2010 by the World Meteorological Organization.